ADVANCED FUNCTIONAL MATERIALS
www.afm-journal.de

Robust π-Conjugated Hydrogen-Bonded Organic Framework Nanowires Enable Stable and Fast Potassium Storage

Kang Han, Chaoqiang Tan, Sicheng Feng, Qi Zhang, Xinying Qiao, Zhenhang Zhong, Xuanpeng Wang, Jiashen Meng, and Liqiang Mai**

Organic cathodes are considered promising energy storage materials in potassium ion batteries (KIBs) due to their molecular flexibility, cost-effectiveness, and sustainability. However, challenges such as high solubility and slow reaction kinetics hinder the development of organic molecules for KIBs. Herein, a novel in situ self-assembly strategy is presented to construct a robust hydrogen-bonded organic framework cathode (H-NDA-G) with extensive π-conjugated systems and excellent chemical stability. By selecting 2,4-diaminotriazine as the connecting ligand, which serves both as a hydrogen bond donor and acceptor, the H-NDA-G cathode is constructed utilizing its amide reaction with dianhydride and the strong π–π adsorption interactions with graphene oxide (GO). The weak electronic coupling between H-NDA-G not only provides charge transfer channels within the framework but also forms an interconnected conductive network through hydrogen bonding and π–π adsorption with the GO, facilitating the redox reactions of K^+ within the H-NDA-G electrode. Consequently, the H-NDA-G cathode exhibits extraordinary performance with a high capacity (120 mAh g^{-1} at 0.1 A g^{-1}) and cycle life exceeding 1000 cycles at 1 A g^{-1}, demonstrating significant potential for practical applications. This study underscores the potential to enhance the potassium storage capability of organic cathodes by modulating intermolecular forces toward efficient and sustainable KIBs.

1. Introduction

Lithium-ion batteries (LIBs) have been extensively applied across various energy storage devices. However, the accelerated commercialization processes have resulted in rapid depletion and market price increases for lithium resource.[1–3] Therefore, developing alternative technologies for LIBs has become an urgent necessity. Given the similar chemical properties shared by potassium (K) and lithium (Li), both situated in the first group of the periodic table, and considering the abundant presence of K in the Earth's crust (2.36 wt.%), potassium-ion batteries (KIBs) have garnered significant attention within the industry.[4–6] The standard hydrogen electrode potential for K is −2.93 V, closely aligned with lithium's −3.04 V and lower than sodium's −2.71 V, suggesting potential for KIBs to achieve energy densities and redox potentials comparable with those of LIBs.[7,8] Further studies have revealed that the Lewis acidity for K^+ is lower than that for Na^+ and Li^+, which benefits the enhancement of the migration rate and transference number for K^+ in liquid electrolytes.[9] These advantages indicate the potential of KIBs as an alternative in the energy storage field to LIBs.

However, research on KIBs is not as advanced as it is for LIBs. A scientific challenge hindering the progress of KIBs is the larger ionic radius of K^+ (1.38 Å, compared to 0.76 Å for Li^+ and 1.02 Å for Na^+), which presents difficulties in designing inorganic materials that can reversibly accommodate such large ions within rigid

K. Han, C. Tan, S. Feng, Q. Zhang, X. Qiao, Z. Zhong, J. Meng, L. Mai
State Key Laboratory of Advanced Technology for Materials Synthesis and Processing
School of Materials Science and Engineering
Wuhan University of Technology
Wuhan 430070, P. R. China
E-mail: jsmeng@whut.edu.cn; mlq518@whut.edu.cn

K. Han, X. Wang, J. Meng, L. Mai
Hubei Longzhong Laboratory
Wuhan University of Technology (Xiangyang Demonstration Zone)
Xiangyang, Hubei 441000, P. R. China

X. Wang
Department of Physical Science & Technology
School of Physics and Mechanics
Wuhan University of Technology
Wuhan 430070, P. R. China

X. Wang, J. Meng
Zhongyu Feima New Material Technology Innovation Center (Zhengzhou) Co., Ltd.
High Technology Industrial Development Zone
No. 60 Xuelan Road, Zhengzhou, Henan 450001, China

The ORCID identification number(s) for the author(s) of this article can be found under https://doi.org/10.1002/adfm.202407452

DOI: 10.1002/adfm.202407452

and confined frameworks.[10,11] Organic electrode materials have emerged as promising alternatives for KIBs due to their inherent advantages of high sustainability, cost-effectiveness, and tunable electrochemical properties.[12–15] Despite the advantages of organic cathodes, they still face challenges with the irreversible dissolution of small molecules and slow reaction kinetics.[16,17] Various approaches have been employed to address these issues. One viable strategy involves converting small molecular into high molecular polymers through polymerization reactions, including traditional polymerization, metal-organic coordination (MOFs),[18–22] and covalent organic frameworks (COFs).[15,16,23–26] However, these methods often face issues such as complex synthesis processes, insufficient active sites, and low structural crystallinity.

Beyond covalent bonds, organic building blocks can also self-assemble via weak hydrogen bonds to form ordered frameworks, known as Hydrogen-bonded Organic Frameworks (HOFs). HOFs typically exhibit highly porous structures with various channels and voids between molecules, leading to more flexible molecular arrangements and lower ion diffusion repulsion.[22,27–29] Importantly, HOFs can self-assemble into ordered 1D or 2D structures, suppressing small molecule dissolution while enabling more efficient and directional charge transport.[30] Moreover, compared to electrode materials that rely on intercalation, alloying, or conversion mechanisms, HOF materials typically possess abundant C═O active sites, which can facilitate energy storage through redox reactions with K^+, effectively alleviating the spatial hindrance issue caused by the large ionic radius of K^+. However, the weak hydrogen bonds in HOFs are prone to breakage, making HOFs extremely unstable in solutions and challenging to maintain structural integrity, thereby significantly limiting their application in electrochemical energy storage.[31–34] Constructing HOFs materials that possess structural stability, high rate capability, and abundant active sites remains a significant challenge in the development of KIBs.

In this work, we present a novel in situ self-assembly strategy to construct a highly stable HOF composite cathode (denoted as H-NDA-G) that combines an extensive π-conjugated system and exceptional chemical stability. By selecting the nitrogen-rich heterocycle 2,4-diaminotriazine (DAT) as the connecting ligand, the H-NDA-G cathode is constructed through its amide reaction with dianhydride and strong π–π adsorption with graphene oxide (GO). DAT's rich amine groups not only expand the conjugated plane to enhance dynamic charge transfer but also serve as both hydrogen bond donors and acceptors to stabilize the composite HOFs. Experimental and theoretical analyses demonstrate that the weak electronic coupling in H-NDA-G provides charge transfer pathways within its framework and forms a 3D interconnected conductive network with GO through hydrogen bonding and π–π interactions, which facilitates the redox reactions of K^+ within the H-NDA-G electrode. Consequently, the H-NDA-G cathode exhibits outstanding performance with a high capacity of 120 mAh g^{-1} at 0.1 A g^{-1} and a cycle life of over 1000 cycles at 1 A g^{-1}, showcasing significant potential for practical applications. This study emphasizes the potential to enhance potassium storage capacity in organic cathodes through molecular interaction modulation, paving the way for the development of efficient and sustainable KIBs and other multivalent ion technologies.

2. Results and Discussion

The synthesis processes of the H-NDA and H-NDA-G, are conducted through a straightforward in situ self-assembly strategy. In this process, the nitrogen-rich heterocyclic compound 3,5-diamino-1,2,4-triazole (DAT), anhydrides (NTCDA), and graphene oxide (GO) are utilized to construct the H-NDA-G cathode via hydrogen bonding and π–π interactions (**Figure 1a**). Surface electrostatic potential analysis indicates that the amino groups (—NH_2) on the DAT triazole ring and the C—O bonds (O═C—O—C═O) in NTCDA exhibit nucleophilic and electrophilic properties, respectively (Figure S1, Supporting Information). Under solvothermal conditions, C—O reacts with -NH_2 via a nucleophilic addition reaction to generate amide structural units (O═C—N—C═O). Simultaneously, due to the presence of multiple -NH_2 groups in DAT's triazole ring, unreacted -NH_2 groups can serve as strong hydrogen bond donors (N—H···O, N—H···N) (Figure S2a, Supporting Information). These donors can form stable hydrogen bonds with both neighboring amide structural units and oxygen-containing functional groups on GO, thereby self-assembling into 1D nanowires structure (H-NDA) and their derivatives (H-NDA-G) in solution (Figure S2b, Supporting Information). Additionally, the aromatic ring of H-NDA can tightly adhere to the large π-conjugated of GO through π–π stacking interactions.[35] The resulting H-NDA nanowires, ≈50 nm in diameter, exhibit a distinct morphology compared to the rod-like structures of NTCDA and the flake-like structures of DAT (Figure 1b; Figures S3 and S4, Supporting Information). TEM images clearly show that GO is not merely mixed with H-NDA but is closely attached to it through directed self-assembly (Figure 1c). High-resolution TEM images also display clear lattice fringes with a spacing of 3.6 Å (Figure 1d,e; Figure S5, Supporting Information), consistent with the π–π stacking distances observed in common organic molecules and corroborated by theoretical simulations (Figure S6, Supporting Information).[36–39] Selected area electron diffraction (SAED) patterns (Figure 1d, inset figure) reveal distinct single-crystal diffraction spots, providing evidence of the high crystallinity of H-NDA-G. Energy-dispersive X-ray spectroscopy (EDS) also confirms the successful incorporation of the imide structure, as evidenced by the uniform distribution of C, N, and O in H-NDA and H-NDA-G (Figures S7 and S8, Supporting Information). In summary, H-NDA-G exhibits a unique architecture characterized by extensive π-conjugation and multiple hydrogen bonding. Using the H-NDA small molecule as the basic structural unit, each molecule connects to four neighboring molecules through N—H···N hydrogen bonds, extending into a 2D layer in the horizontal plane (Figure 1f). Each 2D layer forms a 3D interconnected conductive network "HOF-GO—HOF" through hydrogen bonding and π–π adsorption with GO. The interlayer spacing is ≈3.6 Å (Figure 1g). The presence of hydrogen bonds and π–π stacking in H-NDA is clearly visualized by the Interaction Region Indicator (IRI) plane-fill plots (Figure 1h; Figures S9 and S10, Supporting Information). Similarly, the strong π–π interactions between H-NDA and GO in H-NDA-G are also clearly evident, providing direct visual evidence of the extensive π-conjugation and multiple hydrogen bonding within H-NDA-G (Figure S11, Supporting Information).

X-ray diffraction (XRD) patterns revealed significant diffraction peaks at 12.5° and 25.1° in H-NDA-G, corresponding to the

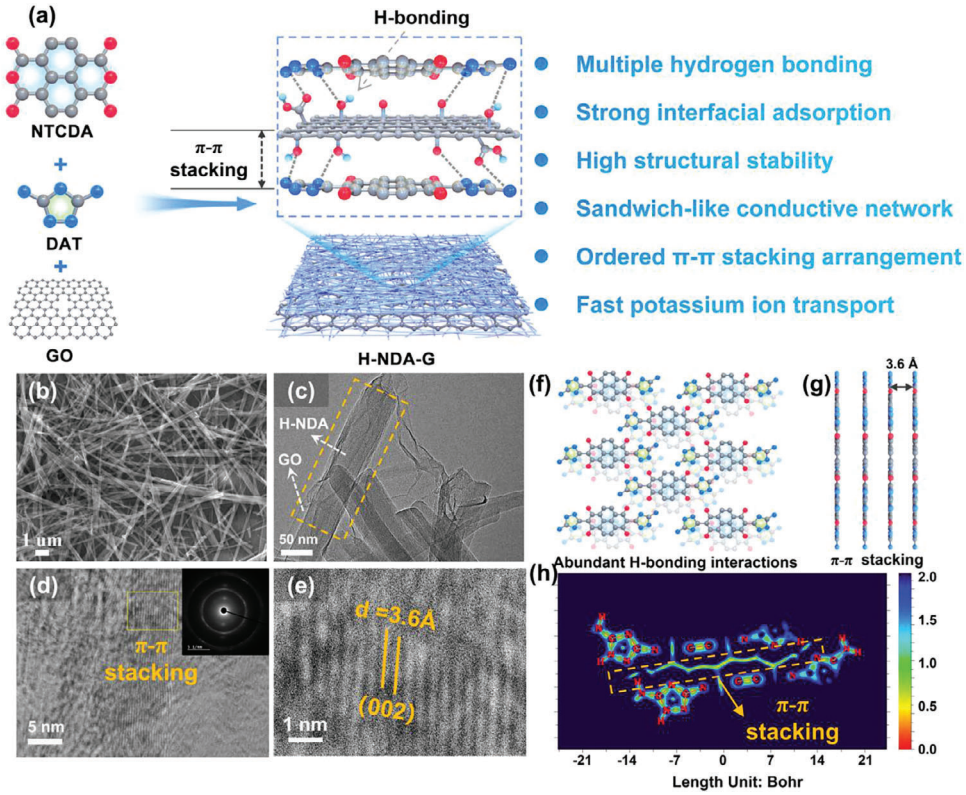

Figure 1. Schematic Illustration of Electrode Synthesis Process and Structural Characterizations of the H-NDA-G. a) The synthesis and structural characteristics of the H-NDA-G. b,c) Scanning Electron Microscopy images of H-NDA-G (b) TEM images of H-NDA-G (c). d,e) HRTEM image of H-NDA-G (the inset image is an electron diffraction pattern) (d) and localized diffraction peaks (e). f,g) Schematic representation of H-NDA constructed via hydrogen bonding and π–π stacking, in planar view (f) and vertical view (g). h) Planar color map of H-NDA based on interaction area indicator function analysis.

(001) and (002) crystal planes. These peaks are similar to those observed in compounds derived from phthalimide derivatives, indicating strong π–π stacking interactions (**Figure** 2a).[36,40] The presence of diffraction peaks at $2\theta = 7.6°$ and 15.2° could be attributed to hydrogen bond interactions, as these bonds typically have lengths between 2.5 Å and 3.0 Å and result in weaker diffraction peaks.[27,41] Compared to H-NDA and GO, H-NDA-G did not exhibit significant phase structural changes, indicating that GO tends to physically adsorb without affecting the crystalline structure of H-NDA (Figure S12a,b, Supporting Information). The similarity in the infrared spectra of H-NDA and H-NDA-G further corroborates this conclusion. Moreover, the presence of new vibration peaks at 1350 cm^{-1} in H-NDA compared to NTCDA indicates the formation of amide bonds. The range of 3000–3500 cm^{-1} in infrared spectra confirms the existence of hydrogen bonding (Figure 2b).[42] Raman spectra of H-NDA-G display a distinct D/G peak, suggesting the incorporation of GO. Significant vibration signals at 1059, 1409, 1607, and 1726 cm^{-1} in both H-NDA and H-NDA-G correspond to V_{N-H}, V_{C-N-C}, $V_{-CO-N-CO-}$, and $V_{C=O}$ molecular vibrations, respectively, further affirming the wide presence of hydrogen and amide bonds (Figure 2c).[42] In situ thermal analysis, along with mass spectrometry and infrared spectroscopy (TG-MS-IR synchronous test), highlights the influence of hydrogen bonds in controlling molecular structure and stability (Figure 2d–f). Thermal decomposition of the H-NDA and H-NDA-G electrodes starts above 400 °C, later than NTCDA and DAT molecules, demonstrating enhanced thermal stability (Figure 2d). The decomposition process reveals an early -NH_2 signal peak, preceding the breakdown of the benzene ring linked by amide bonds. This is because amide formation between NTCDA and DAT uses only one —NH_2 group in DAT, leaving others linked through hydrogen bonds, which decompose first under heat (Figure 2e,f). Furthermore, solid-state ^{13}C nuclear magnetic resonance (^{13}C CP/MAS NMR) identifies characteristic peaks of NTCDA and DAT. The peak at 165 ppm signifies the C═O in the imide ring, while peaks between 140–120 ppm correspond to carbons in the benzene ring, further indicating the structural features resulting from the amidation reaction between NTCDA and DAT (Figure 2g). CHNO analysis confirms the expected elemental composition of H-NDA monomers, ensuring sample purity and accuracy (Figure 2h). XPS analysis showed that both H-NDA and H-NDA-G exhibited distinct N1s signal peaks (Figure 2i), and the high-resolution C1s, O1s, and N1s spectra also indicated the weakening of the C—O peaks and the formation of C═N bonds, and the formation of the amide structure in H-NDA and H-NDA-G (Figures S13 and S14, Supporting Information).

The potential application of the H-NDA and H-NDA-G cathodes in KIBs was further explored. Typical CV curves prove that, compared to NTCDA, both H-NDA, and H-NDA-G possess more significant structural stability and electrochemical reversibility (**Figure** 3a; Figure S15a,b, Supporting Information). The two pairs of redox peaks in the CV curve suggest the transfer of

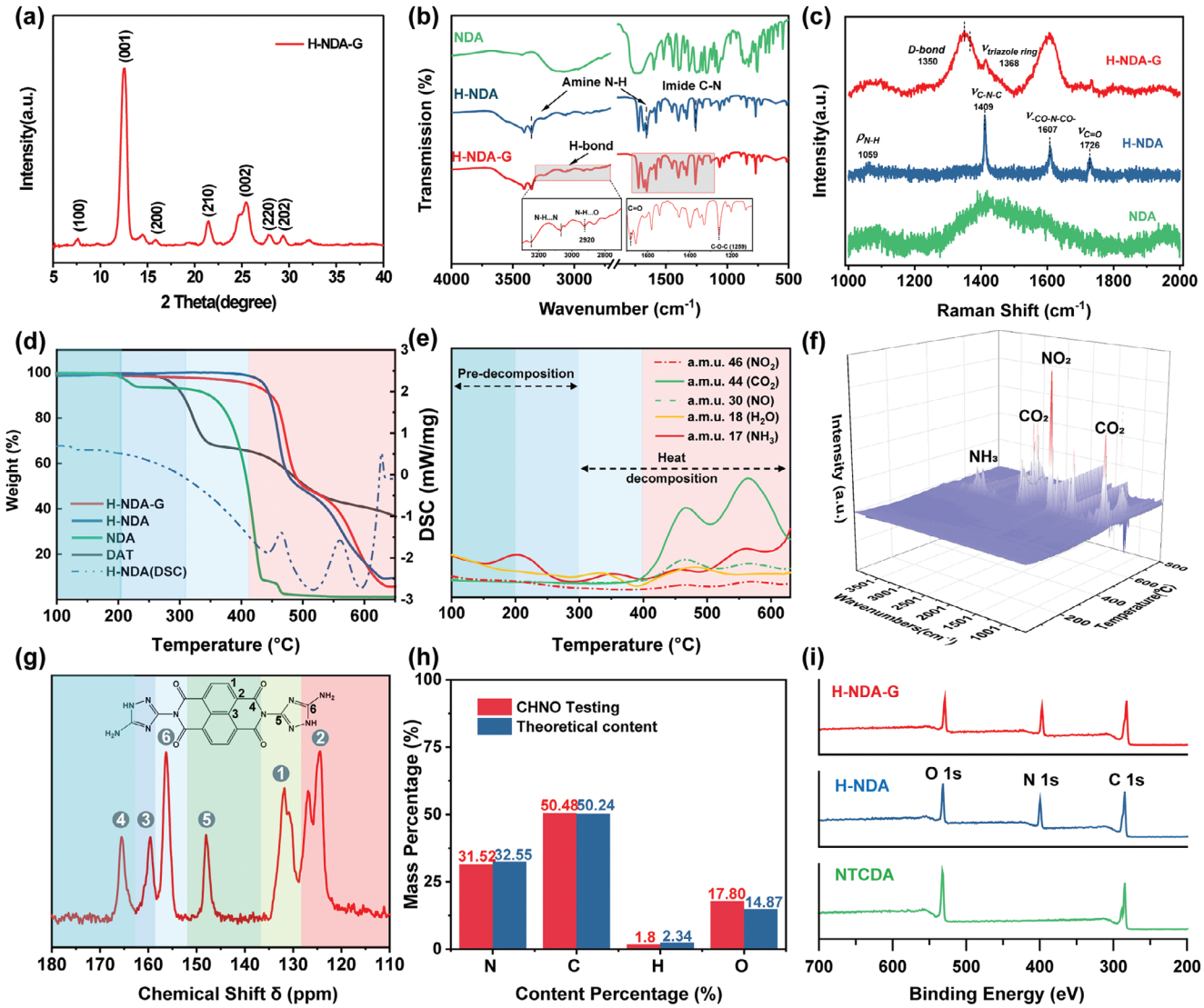

Figure 2. Intrinsic Structural Characteristics of the H-NDA and H-NDA-G samples. a) XRD pattern of the H-NDA-G. b) Comparative infrared spectra of the NDA, H-NDA, and H-NDA-G. c) Raman spectroscopy comparison of the NDA, H-NDA, and H-NDA-G. d–f) TG-MS-IR synchronous test. d) TG curve. e) MS of the H-NDA-G during thermal decomposition. f) IR spectrum of the H-NDA-G during the thermal decomposition process. g) ^{13}C Solid-State NMR spectrum of the H-NDA-G. h) Comparative analysis of molecular structure theory and CHNO test proportions. i) X-ray Photoelectron Spectroscopy (XPS) wide-spectrum comparison of NDA, H-NDA, and H-NDA-G.

two electrons during the electrochemical reaction, corresponding to a high theoretical capacity of 125 mAh g^{-1}. The typical charge–discharge curves of H-NDA and H-NDA-G also indicate that they exhibit extremely high cyclic stability and reversibility in the first five cycles, with discharge-specific capacities of 110 and 120 mAh g^{-1} at 100 mA g^{-1}, respectively, while NTCDA rapidly decays after the first cycle (Figure 3b; Figure S16a,b, Supporting Information). Simultaneously, the polarization voltages of H-NDA-G and H-NDA are ≈0.33 and 0.75 V, respectively, indicating that the introduction of GO and π–π enhancement greatly facilitate electron transport (Figure 3c). After 100 cycles at 100 mA g^{-1}, H-NDA-G still maintains a high reversible specific capacity of 110 mAh g^{-1}, with a capacity retention rate of up to 93% and a Coulombic efficiency of up to 100%. (Figure 3d). Rate performance of the H-NDA-G electrode further highlighted its exceptional electrochemical resilience. The capacities were maintained between 127 and 108 mAh g^{-1} when the current density varied from 50 to 1000 mA g^{-1}. Remarkably, when the current was reset to 50 mA g^{-1}, the capacity of the H-NDA-G electrode fully recovered to 127 mAh g^{-1}, indicating its superior reactivity and stability (Figure 3e). The charge–discharge curves at different current densities consistently maintain similar electrochemical plateaus, further indicating that H-NDA-G possesses rapid reaction kinetics and excellent power characteristics (Figure 3f). Long-term cycling tests demonstrate the exceptional cycling stability of H-NDA-G. At a high current density of 1 A g^{-1}, H-NDA-G delivers a remarkable capacity of 102 mAh g^{-1} and still retains 70% of its capacity after 1000 cycles (Figure 3g). Notably, despite exhibiting inferior cycling performance compared to H-NDA-G, H-NDA still represents a significant improvement over NTCDA.

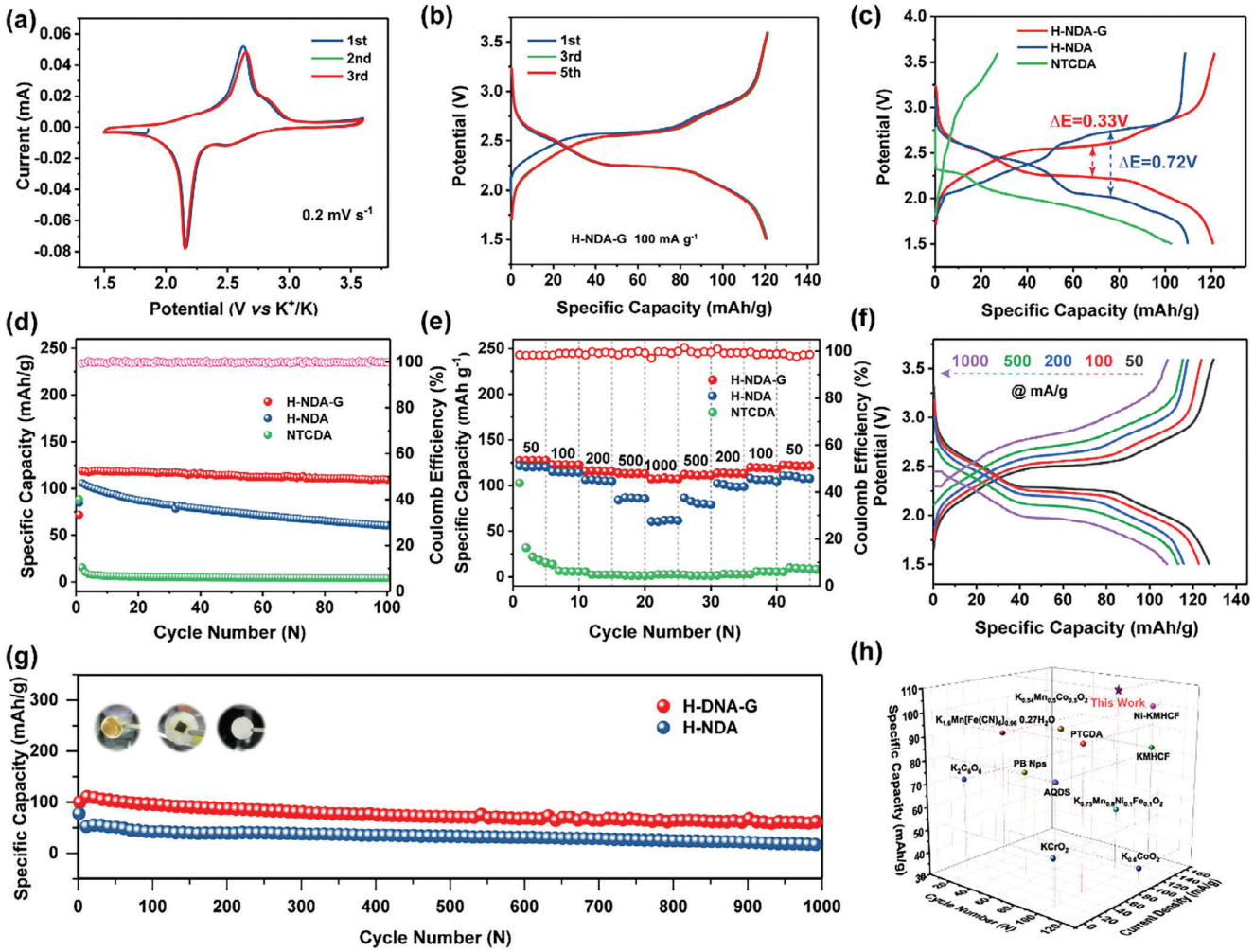

Figure 3. Electrochemical performances of NDA, H-NDA, and H-NDA-G. a) Typical CV curves of H-NDA-G at a scan rate of 0.2 mV s^{-1}. b) Comparison of characteristic charge–discharge curves of NDA, H-NDA, and H-NDA-G. c) Polarization voltage characterization of typical charge/discharge curves of H-NDA-G, H-NDA, and NTCDA. d) First 100-cycle discharge specific capacity of NDA, H-NDA, and H-NDA-G at 100 mA g^{-1}. e) Rate performance of NDA, H-NDA, and H-NDA-G. f) Charge–discharge curves of H-NDA-G at different charging/discharging currents. g) Long-term cycling performance comparison of H-NDA and H-NDA-G at 1 A g^{-1} (Inset figure, Photographs of the membranes after 100 cycles of NDA, H-NDA, and H-NDA-G, respectively.) h) 3D comparison graph of electrochemical performance of H-NDA-G with conventional cathodes reported currently.

This performance disparity may stems from the multi-hydrogen bonding structure in H-NDA and H-NDA-G, which effectively suppresses the dissolution of small molecules during cycling. Post-cycling membrane images clearly reveal that while NTCDA undergoes significant dissolution, H-NDA and H-NDA-G remain intact, showcasing their superior stability (Figure 3g, insert figure; Figure S17, Supporting Information). Solubility tests in different solvents also confirm the remarkable stability of H-NDA and H-NDA-G, as they remain largely intact after 30 days immersion, while NTCDA exhibits noticeable dissolution in all solvents except water (Figure S18, Supporting Information). The ion diffusion capabilities of H-NDA and H-NDA-G were evaluated using the galvanostatic intermittent titration (GITT) technique. The ion diffusion coefficient of H-NDA-G is $\approx 4 \times 10^{-11}$, slightly higher than that of H-NDA, which is $\approx 1.8 \times 10^{-12}$ (Figures S19 and S20, Supporting Information). Electrochemical impedance spectroscopy (EIS) at different charging and discharging stages was also employed to study the information related to charge storage under dynamic conditions for both materials. The diameter of the semicircles in the high-frequency region for both decreases as charging progresses, confirming that charge storage in these two materials is accompanied by a rapid charge transfer process (Figure S21, Supporting Information). Meanwhile, the impedance of H-NDA-G is significantly lower than that of the H-NDA electrode, corresponding to an improvement in conductivity. To our knowledge, the H-NDA and H-NDA-G cathodes provide a new example of designing and validating high-rate rechargeable potassium organic batteries from the perspective of constructing intermolecular secondary bonds. The fabricated H-NDA-G cathode surpasses most previously reported potassium organic battery cathodes in terms of reversible specific capacity and cycling stability (Figure 3h).[4,43–51]

In situ XRD and in situ Raman spectroscopy were jointly employed to elucidate the differences in the energy storage

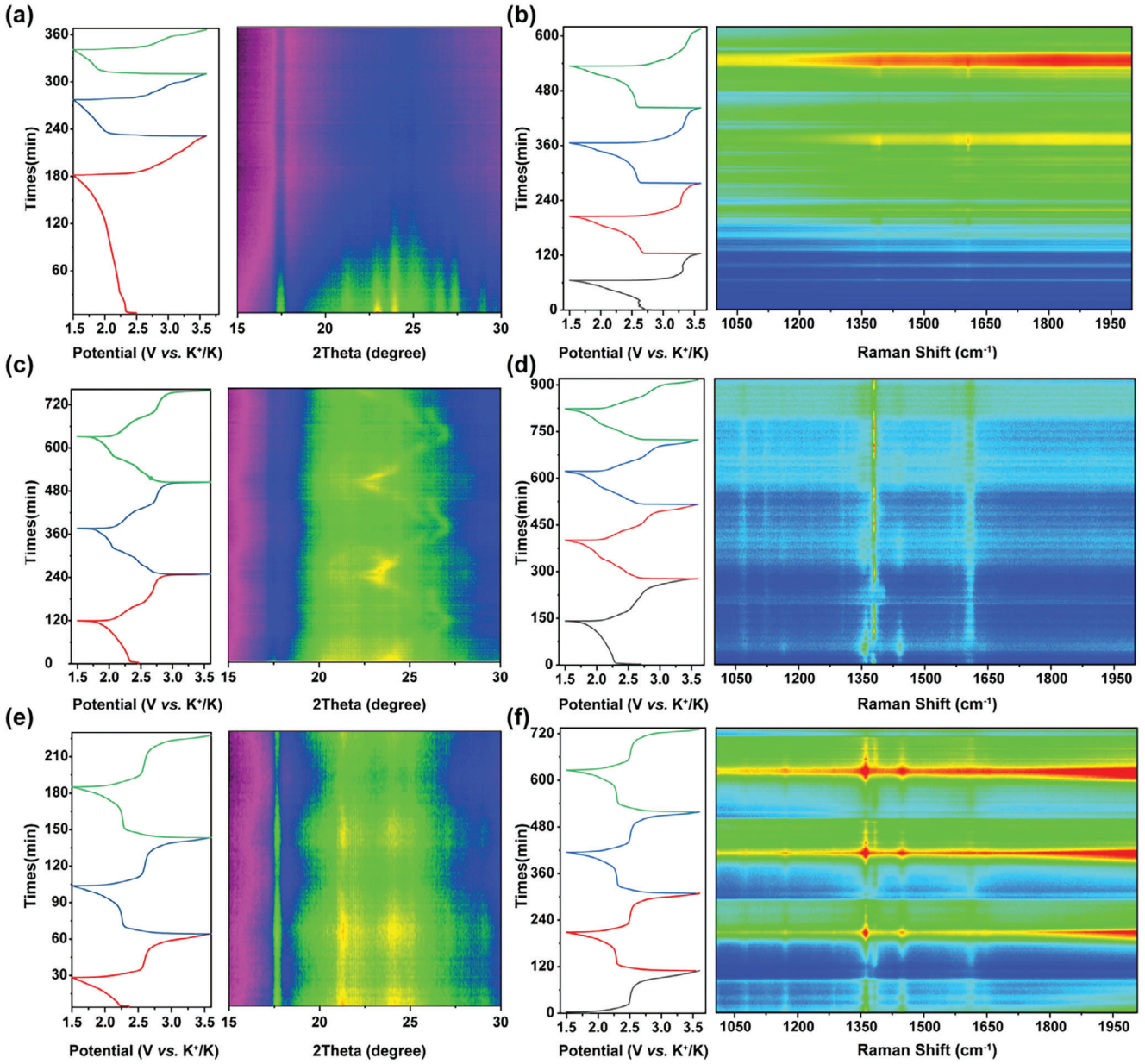

Figure 4. In situ XRD and in situ Raman tests of the NDA, H-NDA, and H-NDA-G. a) In situ XRD of NDA. b) In situ Raman of NDA. c) In situ XRD of H-NDA. d) In situ Raman of H-NDA. e) In situ XRD of H-NDA-G. f) In situ Raman of H-NDA-G.

mechanisms of the cathodes in H-NDA and H-NDA-G. In situ XRD and Raman spectra for NTCDA showed that its characteristic peaks gradually weakened and eventually vanished during the first discharge cycle, indicative of the irreversible charging and discharging process observed in the charge–discharge curves (**Figure** 4a,b). In contrast, for H-NDA, the charging and discharging process led to a notable periodic expansion/contraction of interlayer distances in the in situ XRD spectra, suggesting the presence of an interlayered structure in H-NDA and a reversible intercalation/deintercalation in the bulk H-NDA phase (Figure 4c). For H-NDA-G, the periodic changes in interlayer distance observed in H-NDA were absent, replaced by significant phase reactions (Figure 4e), corresponding to the disappearance of the 2.1/2.5 V CV peak in H-NDA-G. The in situ Raman analysis further highlighted the distinctions between H-NDA and H-NDA-G regarding bulk phase intercalation versus interface decoupled transport. In H-NDA, the vibration peak at 1380 cm^{-1}, related to the vibration of nitrogen-containing five-membered heterocycles, showed periodic changes with charging and discharging (Figure 4d). A comparison of the Raman spectra between H-NDA and H-NDA-G revealed a noticeable shift in the vibrational center from 1380 to 1360 cm^{-1}, corresponding to the disordered or defect-induced D peak in GO (Figure 4f). The shift in Raman peaks can be attributed to the presence of surface defects and edges in the interface graphene layers of H-NDA-G, which enhances the adsorption of K^+ and

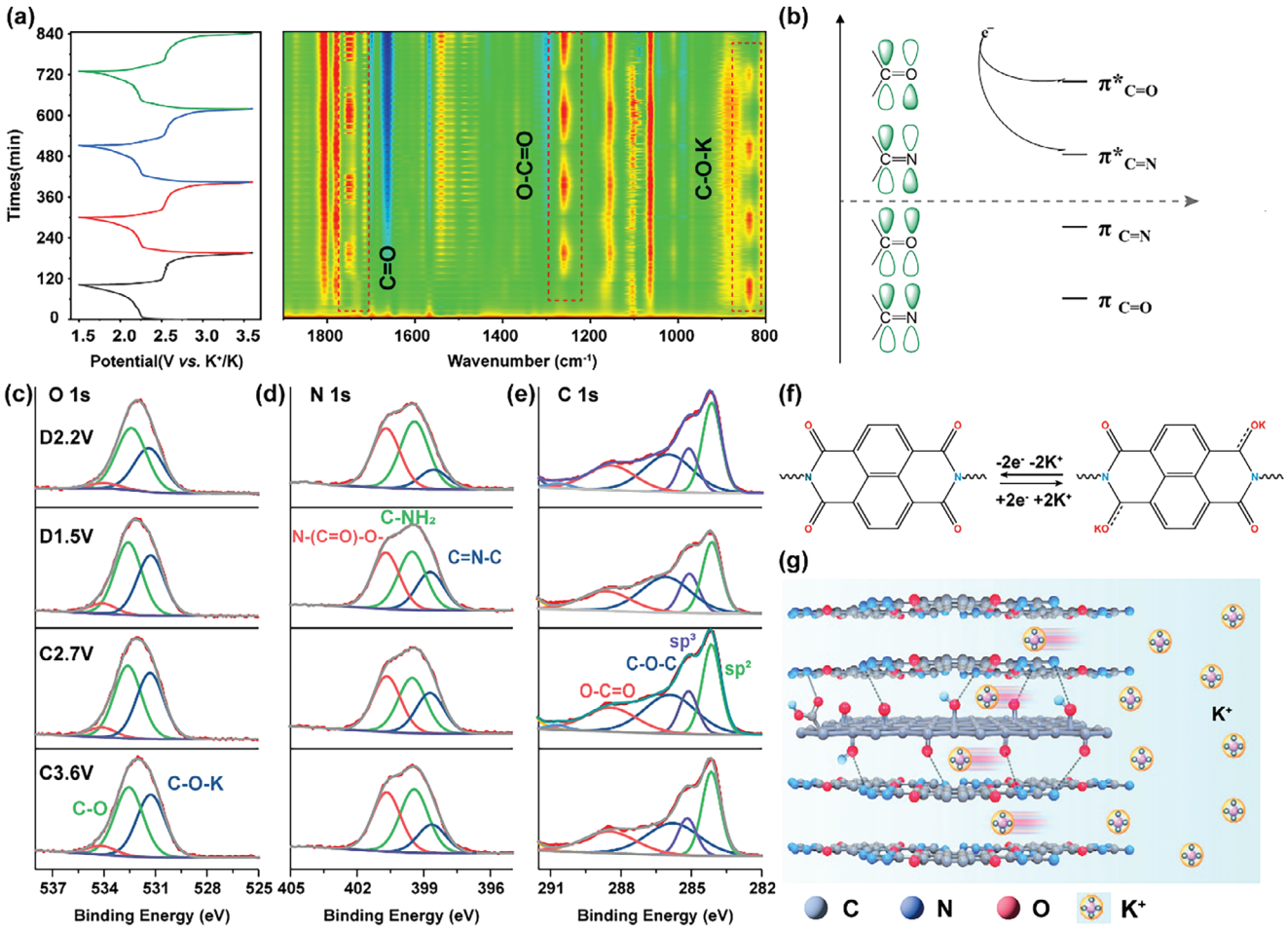

Figure 5. Identification of the potassium storage mechanism in the H-NDA-G. a) Evolution of in situ infrared peaks corresponding to the first four cycles of H-NDA-G. b) Schematic Diagram of energy levels of molecular orbitals for C═O and C═N. c–e) Evolution of XPS signal peaks of H-NDA-G at different potentials. c) O1s spectrum, d) N1s spectrum, e) C1s spectrum. f) Reaction mechanism of H-NDA-G. g) Schematic representation of potassium storage in H-NDA-G based on interface decoupling.

their decoupled transport at the interface, leading to rapid kinetics.

The in situ Fourier Transform Infrared (FT-IR) spectroscopy of H-NDA-G reveals that during the discharge process, the peaks corresponding to C—O and C═O groups at 1280 and 1700–1800 cm^{-1} respectively diminish rapidly, while a new peak emerges at 828 cm^{-1}, indicating the formation of C—O—K (**Figure** 5a). As charging progresses, the C—O—K peak disappears, and the C═O and C—O peaks reappear, demonstrating the characteristics of —C═O Faradaic reactions in H-NDA-G, which exhibit high structural stability and reversible K^+ storage capabilities. In contrast, the in situ FT-IR spectra of H-NDA do not exhibit a significant change in the C═O peak (Figure S22, Supporting Information), likely attributed to the dominant role of intercalation reactions in H-NDA's reversible potassium storage, consistent with the observations from in situ XRD (Figure 4c). The marked difference in the C═O peaks suggests that H-NDA-G significantly facilitates the —C═O Faradaic reactions compared to H-NDA. Molecular orbital theory also indicates the sequence of electron gain and loss in H-NDA-G as $\pi^*_{C=O} > \pi^*_{C=N} > \pi_{C=N} > \pi_{C=O}$ (Figure 5b), further verifying the —C═O Faradaic process in H-NDA-G. XPS results reveal that at a discharge to 1.5 V, the initial C═O peak at 531.5 eV splits into a C—O—K signal peak (531.2 eV) and a C—O peak (533 eV). Upon charging to 3.6 V, as the C═O peak recovers, the intensity of the C—O—K signal peak decreases (Figure 5c; Figure S23a, Supporting Information). Throughout the charge–discharge cycle, no significant changes are observed in the N spectra of either material, reaffirming the K storage characteristics of the C═O functionality in H-NDA-G (Figure 5d; Figure S23b, Supporting Information). Meanwhile, no notable changes are observed in the C spectra of H-NDA-G during charging and discharging, whereas significant variations are noted in the C spectra of H-NDA (Figure 5e; Figure S24, Supporting Information). This likely results from the π–π conjugated structures within the heterostructure of H-NDA-G effectively enhancing electron transmission between the bulk phase and the surface interface, thereby reducing localized reactions caused by charge accumulation. Moreover, rapid electron transmission facilitates the —C═O Faradaic reactions within H-NDA-G while simultaneously restricting the progression of intercalation reactions, further enhancing structural stability (Figure 5f,g).

The enhancement principle of electronic and ionic transport properties in H-NDA-G can be described by the classical Nernst-Planck equation combined with the charge conservation principle, where the transport of electrons and ions in the H-NDA-G heterostructure is described as two independent processes occurring in different phases[61]. Here, H-NDA serves as phase α, while GO is denoted as phase β, with their combined flux expression for electrons and ions described as follows (Deduction method referring to Note S1, Supporting Information):

$$j_M = -\frac{1}{F^2}\left(\frac{\sigma^{\alpha}_{ion}\sigma^{\beta}_{eon}}{\sigma^{\alpha}_{ion}+\sigma^{\beta}_{eon}}\right)\left(\nabla\mu^{\alpha}_{ion}+\nabla\mu^{\beta}_{eon}+F\left(\phi^{\alpha}-\phi^{\beta}\right)\right) \quad (1)$$

Clearly, in the aforementioned formula, the total charge carrier flux j_M is driven by the combined electrochemical potential gradients of ions and electrons. In the H-NDA-G system, rGO provides high electron conductivity, while the 1D nanowire structure of H-NDA offers channels for ion storage and migration (Figure 5g). Hence, it can be anticipated that the value of $\frac{\sigma^{\alpha}_{ion}\sigma^{\beta}_{eon}}{\sigma^{\alpha}_{ion}+\sigma^{\beta}_{eon}}$ will increase. Additionally, the term $F(\phi^{\alpha}-\phi^{\beta})$ equals zero in a homogeneous structure but forms a potential difference at the interface in the H-NDA-G heterostructure. This indicates that the heterostructure design, based on π–π conjugated, optimizes the transport of electrons and ions, thereby enhancing the overall electrochemical performance. Multi-scan rate CV measurements provided further evidence to distinguish the difference between bulk diffusion and interface diffusion mechanisms for H-NDA and H-NDA-G (Figures S25 and S26, Supporting Information). The peak currents of H-NDA and H-NDA-G at various scan rates were measured and analyzed using the power-law formula $i = av^b$. The calculated b values for H-NDA and H-NDA-G are 0.64 and 0.92, respectively (Figures S25c and S26c, Supporting Information). These values suggest that K^+ transport in H-NDA is predominantly diffusion-controlled, whereas, in H-NDA-G, it demonstrates characteristics of both diffusion and surface-controlled processes. Further, the analysis of the capacitance ratio revealed that H-NDA-G consistently exhibits a significantly higher capacitance ratio than the H-NDA electrode across various scan rates, suggesting that the superior interface energy storage capabilities of H-NDA-G (Figures S25d and S26d, Supporting Information). Ex situ SEM was also employed to observe their morphology changes of H-NDA and H-NDA-G during cycling. H-NDA cathodes exhibited distinct micron-sized flower-like and sheet-like structures after 100 and 200 cycles, respectively (Figure S27, Supporting Information). This morphological transformation is likely attributed to deposition/dissolution side reactions involving H-NDA during cycling. The presence of interfacial side reactions further induced structural degradation of H-NDA. In contrast, H-NDA-G retained its well-defined nanowire structure even after 200 cycles, with only slight surface passivation. This observation also suggests that the incorporation of GO not only enhances conductivity but also provides interfacial protection for H-NDA, effectively suppressing deep dissolution of the H-NDA cathode.

Theoretical calculations further elucidated the electronic structure and intrinsic properties of H-NDA and H-NDA-G. HOMO—LUMO energy level analysis revealed that the energy gaps for DAT, NTCDA, H-NDA, and H-NDA-G are 6.17, 3.69, 3.24, and 0.45 eV, respectively (Figure S28, Supporting Information). The energy gap of DAT is significantly larger than that of NTCDA, and the gap of H-NDA is slightly smaller than that of NTCDA, indicating that the introduction of amide structures further extends the conductivity of the material. H-NDA-G exhibited the smallest energy gap among all materials, further verifying its rapid electron transport characteristics. The electrostatic potential results indicate that the electron-rich region in H-NDA primarily resides near the C═O group, further confirming the storage of cationic carriers (K^+) by oxygen atoms (Figure S29, Supporting Information). Density of states (DOS) analysis for H-NDA and H-NDA-G indicated an increase in the electronic state density at various energy levels for H-NDA-G compared to H-NDA, especially near the Fermi level, suggesting that the addition of GO enhances the conductivity of H-NDA-G (**Figure 6a**). Further orbital component analysis revealed that in H-NDA, the valence band is mostly provided by the nitrogen-containing five-membered heterocycles, while the conduction band is provided by large-conjugated benzene rings (Figure S30a, Supporting Information). In H-NDA-G, the introduction of GO significantly affected the electronic properties, with less impact from phenyl and nitrogen-containing heterocycles (Figure S30b, Supporting Information). This may be because the 2D structure and larger surface area of GO provide more electronic states, while phenyl and nitrogen-containing heterocycles may contribute less due to their relatively smaller structural presence. The migration diffusion barriers of K^+ in H-NDA and H-NDA-G indicate that the migration barrier of K^+ in H-NDA-G (3.08 kcal mol^{-1}) is significantly lower than in H-NDA (30.39 kcal mol^{-1}), with corresponding diffusion barriers of 1.33 and 0.65 eV, respectively, suggesting facilitated migration of K^+ in H-NDA-G (Figure 6b,c). Additionally, the differential charge density plots for K^+ in H-NDA and H-NDA-G highlight pronounced electronic accumulation between K^+ and H-NDA, indicating a strong interaction between K^+ and the surface. In contrast, the charge density accumulation between H-NDA and GO is relatively lower, implying favorable pathways for K^+ diffusion (Figure 6d). This phenomenon may be attributed to the unique "sandwich-like" structure of H-NDA-G, offering abundant active storage sites at the surface and interface, while its weak electronic coupling promotes ultra-fast ion transport and migration within the framework structure.

3. Conclusion

In summary, this study introduces an in situ self-assembly strategy for constructing a highly stable H-NDA-G cathode with an extensive π-conjugated system and excellent chemical stability. By selecting 2,4-diaminotriazine as the connecting ligand, the H-NDA small molecule was synthesized through its amide reaction with dianhydride. Using the H-NDA small molecule as the basic structural unit, each molecule connects to four neighboring molecules through N—H···N hydrogen bonds, extending into a 2D layer. Each 2D layer forms a highly stable HOF through face-to-face π–π stacking interactions. The weak electronic coupling between H-NDA-G not only provides channels for charge transfer within the framework but also forms a 3D "HOF-GO-HOF Sandwich-like" conductive network through hydrogen bonding and π–π adsorption with GO, enhancing the redox reactions of K^+ in the H-NDA-G electrode. As a result, the

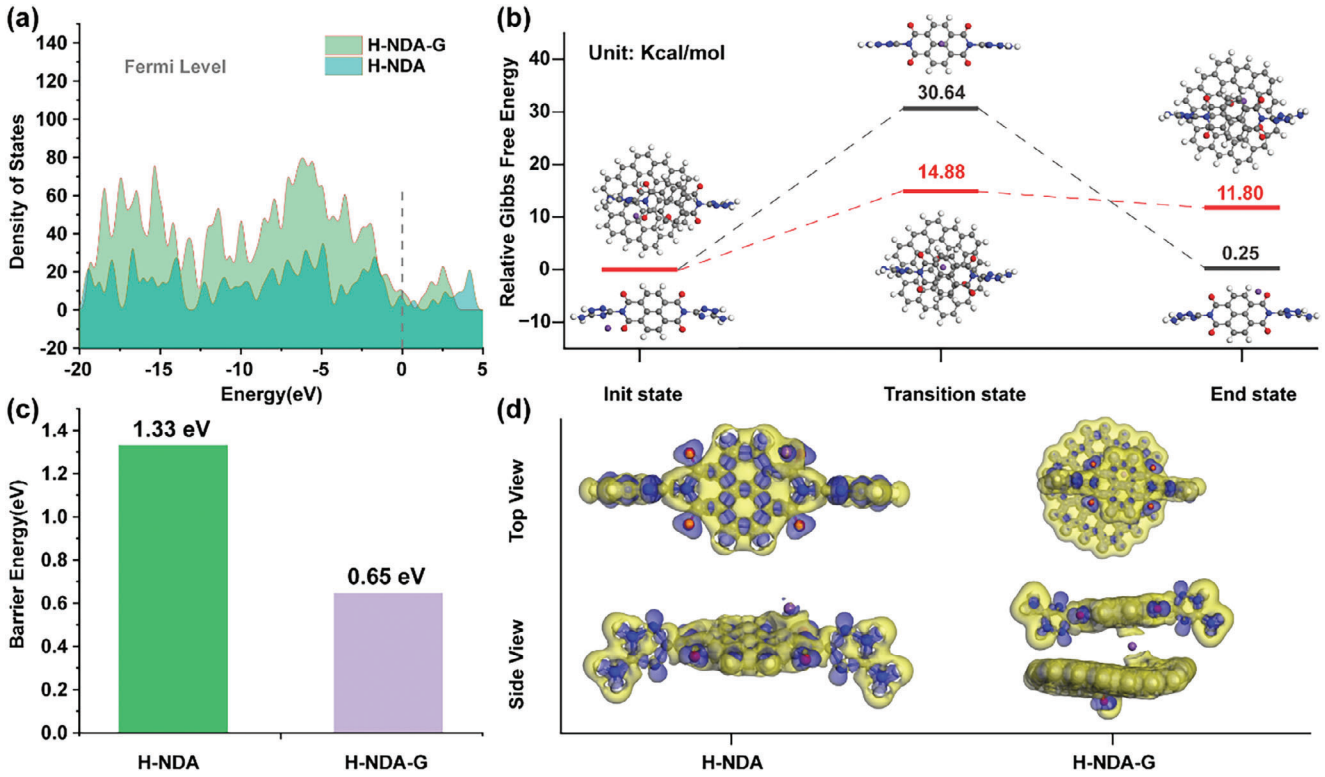

Figure 6. Theoretical investigation of potassium ion adsorption and migration diffusion energy barriers in H-NDA and H-NDA-G. a) Comparison of state densities in H-NDA and H-NDA-G. b) Study of K^+ migration diffusion transition states in H-NDA and H-NDA-G (black line represents H-NDA, red line represents H-NDA-G). c) Comparison of K^+ diffusion migration energy barriers in H-NDA and H-NDA-G. d) Study of K^+ adsorption and charge density differences in H-NDA and H-NDA-G.

H-NDA-G cathode exhibits exceptional performance with a high capacity (120 mAh g^{-1} at 0.1 A g^{-1}) and outstanding cycle life, exceeding 1000 cycles at 1 A g^{-1}, demonstrating significant potential for practical applications. This study emphasizes the potential of enhancing the potassium storage capability of organic cathodes by modulating intermolecular forces, paving the way for the development of efficient and sustainable KIB and other multivalent ion technologies.

Supporting Information

Supporting Information is available from the Wiley Online Library or from the author.

Acknowledgements

This work was supported by the National Key Research and Development Program of China (2023YFB3809300), National Energy-Saving and Low-Carbon Materials Production and Application Demonstration Platform Program (TC220H06N), National Natural Science Foundation of China (52373306, 52472244 and 52127816), Natural Science Foundation of Hubei Province (2023AFA053).

Conflict of Interest

The authors declare no conflict of interest.

Data Availability Statement

The data that support the findings of this study are available from the corresponding author upon reasonable request.

Keywords

π–π conjugation, 1D nanowires, dissolution inhibition, high stability, hydrogen-bonded framework materials, potassium organic batteries

Received: April 30, 2024
Revised: May 21, 2024
Published online: November 8, 2024

[1] E. C. Evarts, *Nature* **2015**, *526*, S93.
[2] Y. Lu, J. Chen, *Nat. Rev. Chem.* **2020**, *4*, 127.
[3] P. Simon, Y. Gogotsi, B. Dunn, *Science* **2014**, *343*, 1210.
[4] H. Kim, J. C. Kim, S. H. Bo, T. Shi, D. H. Kwon, G. Ceder, *Adv. Energy Mater.* **2017**, *7*, 1700098.
[5] X. Zhang, H. Zhu, Q. He, T. Xiong, X. Wang, Z. Xiao, H. Wang, Y. Zhao, L. Xu, L. Mai, *Adv. Funct. Mater.* **2022**, *32*, 2205330.
[6] M. Zhou, P. Bai, X. Ji, J. Yang, C. Wang, Y. Xu, *Adv. Mater.* **2021**, *33*, 2003741.
[7] W. Zhang, J. Yin, W. Wang, Z. Bayhan, H. N. Alshareef, *Nano Energy* **2021**, *83*, 105792.
[8] P. Wu, X. Xu, Y. Wu, F. Xu, X. Wang, J. Meng, C. Han, X. Liu, Z. Zhu, L. Mai, *Adv. Energy Mater.* **2021**, *11*, 2003612.

[9] P. Luo, C. Zheng, J. He, X. Tu, W. Sun, H. Pan, Y. Zhou, X. Rui, B. Zhang, K. Huang, *Adv. Funct. Mater.* **2022**, *32*, 2107277.
[10] X. Ding, Y. Wang, X. Wang, L. Geng, C. Guo, W. Liu, H. Wang, C. Sun, C. Han, *Chem. Eng. J.* **2023**, *466*, 143331.
[11] F. Qiao, J. Wang, Y. Zhu, X. Tan, X. Wang, Q. An, *Chem. Eng. J.* **2022**, *439*, 135777.
[12] G. Vardhini, S. Suriyakumar, M. M. Shaijumon, *ACS Appl. Energy Mater.* **2022**, *5*, 9595.
[13] X. Xue, Y. Zhang, M. Shi, T. Li, T. Huang, J. Qi, F. Wei, Y. Sui, Z. Jin, *Acta Chim. Sin.* **2022**, *80*, 1618.
[14] J. Zou, C. Fu, Y. Zhang, K. Fan, Y. Chen, C. Zhang, G. Zhang, H. Dai, Y. Cao, J. Ma, C. Wang, *Adv. Funct. Mater.* **2023**, *33*, 2303678.
[15] K. Geng, T. He, R. Liu, S. Dalapati, K. T. Tan, Z. Li, S. Tao, Y. Gong, Q. Jiang, D. Jiang, *Chem. Rev.* **2020**, *120*, 8814.
[16] P. Poizot, J. Gaubicher, S. Renault, L. Dubois, Y. Liang, Y. Yao, *Chem. Rev.* **2020**, *120*, 6490.
[17] T. M. Gur, *Energy Environ. Sci.* **2018**, *11*, 2696.
[18] Q. Zhang, S. Jiang, T. Lv, Y. Peng, H. Pang, *Adv. Mater.* **2023**, *35*, 2305532.
[19] T. Zhao, P. Xiao, S. Nie, M. Luo, M. Zou, Y. Chen, *Coordin. Chem. Rev.* **2024**, *502*, 215592.
[20] R. Zhao, Z. Liang, R. Zou, Q. Xu, *Joule* **2018**, *2*, 2235.
[21] M. Zhong, M. Liu, N. Li, X.-H. Bu, *J. Energy Chem.* **2021**, *63*, 113.
[22] C. Zhou, Z. Li, X. Xu, L. Mai, *Natl. Sci. Rev.* **2021**, *8*, nwab055.
[23] J. Wang, H. Jia, Z. Liu, J. Yu, L. Cheng, H.-G. Wang, F. Cui, G. Zhu, *Adv. Mater.* **2023**, *36*, 2305605.
[24] J. Ma, E. Zhou, C. Fan, B. Wu, C. Li, Z.-H. Lu, J. Li, *Chem. Commun.* **2018**, *54*, 5578.
[25] D.-G. Wang, T. Qiu, W. Guo, Z. Liang, H. Tabassum, D. Xia, R. Zou, *Energy Environ. Sci.* **2021**, *14*, 688.
[26] H. Zhang, Y. Fang, F. Yang, X. Liu, X. Lu, *Energy Environ. Sci.* **2020**, *13*, 2515.
[27] G. Gilli, P. Gilli, *The Nature of the Hydrogen Bond: Outline of a Comprehensive Hydrogen Bond Theory*, Oxford University Press, New York, **2009**.
[28] C. Guo, Y. Gao, S.-Q. Li, Y. Wang, X.-J. Yang, C. Zhi, H. Zhang, Y.-F. Zhu, S. Chen, S.-L. Chou, S.-X. Dou, Y. Xiao, X. Luo, *Adv. Funct. Mater.* **2024**, *34*, 2314851.
[29] J. Tang, R. Yang, Y. Peng, H. Lin, X. He, Y. Song, K. Wu, Y. Kang, L. Yang, *Small* **2024**, *20*, 2307827.
[30] B. Wang, R.-B. Lin, Z. Zhang, S. Xiang, B. Chen, *J. Am. Chem. Soc.* **2020**, *142*, 14399.
[31] Y. Wu, R. Zeng, J. Nan, D. Shu, Y. Qiu, S.-L. Chou, *Adv. Energy Mater.* **2017**, *7*, 1700278.
[32] Z. L. Hu, X. L. Zhao, Z. Z. Li, S. Li, P. F. Sun, G. L. Wang, Q. B. Zhang, J. J. Liu, L. Zhang, *Adv. Mater.* **2021**, *33*, 2104039.
[33] Z. Luo, L. Liu, Q. Zhao, F. Li, J. Chen, *Angew. Chem.* **2017**, *56*, 12561.
[34] F. J. M. Hoeben, P. Jonkheijm, E. W. Meijer, A. Schenning, *Chem. Rev.* **2005**, *105*, 1491.
[35] J. Björk, F. Hanke, C.-A. Palma, P. Samori, M. Cecchini, M. Persson, *J. Phys. Chem. Lett.* **2010**, *1*, 3407.
[36] Y. Huang, R. Yuan, S. Zhou, *J. Mater. Chem.* **2012**, *22*, 883.
[37] A. Levin, T. Leisegang, R. Forker, M. Koch, D. Meyer, T. Fritz, *Cryst. Res. Technol.* **2010**, *45*, 439.
[38] L. J. Riwar, N. Trapp, B. Kuhn, F. Diederich, *Angew. Chem. Int. Ed. Engl.* **2017**, *56*, 11252.
[39] A. S. Shetty, J. Zhang, J. S. Moore, *J. Am. Chem. Soc.* **1996**, *118*, 1019.
[40] Y. Huang, Y. Yan, B. M. Smarsly, Z. Wei, C. F. Faul, *J. Mater. Chem.* **2009**, *19*, 2356.
[41] D. Zhao, J. Huang, Y. Zhong, K. Li, L. Zhang, J. Cai, *Adv. Funct. Mater.* **2016**, *26*, 6279.
[42] Y. Wu, X. Mao, M. Zhang, X. Zhao, R. Xue, S. Di, W. Huang, L. Wang, Y. Li, Y. Li, *Adv. Mater.* **2021**, *33*, 2106079.
[43] J.-Y. Hwang, J. Kim, T.-Y. Yu, H.-G. Jung, J. Kim, K.-H. Kim, Y.-K. Sun, *J. Mater. Chem. A* **2019**, *7*, 21362.
[44] C. Zhang, Y. Xu, M. Zhou, L. Liang, H. Dong, M. Wu, Y. Yang, Y. Lei, *Adv. Funct. Mater.* **2017**, *27*, 1604307.
[45] X. Jiang, T. Zhang, L. Yang, G. Li, J. Y. Lee, *ChemElectroChem* **2017**, *4*, 2237.
[46] Y. h. Zhu, Y. b. Yin, X. Yang, T. Sun, S. Wang, Y. s. Jiang, J. m. Yan, X. b. Zhang, *Angew. Chem. Int. Ed. Engl.* **2017**, *56*, 7881.
[47] B. Li, J. Zhao, Z. Zhang, C. Zhao, P. Sun, P. Bai, J. Yang, Z. Zhou, Y. Xu, *Adv. Funct. Mater.* **2019**, *29*, 1807137.
[48] L. Xue, Y. Li, H. Gao, W. Zhou, X. Lü, W. Kaveevivitchai, A. Manthiram, J. B. Goodenough, *J. Am. Chem. Soc.* **2017**, *139*, 2164.
[49] Q. Zhao, J. Wang, Y. Lu, Y. Li, G. Liang, J. Chen, *Angew. Chem. Int. Ed. Engl.* **2016**, *55*, 12528.
[50] Z. Jian, Y. Liang, I. A. Rodríguez-Pérez, Y. Yao, X. Ji, *Electrochem. Commun.* **2016**, *71*, 5.
[51] Y. Chen, W. Luo, M. Carter, L. Zhou, J. Dai, K. Fu, S. Lacey, T. Li, J. Wan, X. Han, *Nano Energy* **2015**, *18*, 205.

